Seismic envelope inversion and modulation signal model

Ru-Shan Wu, Jingrui Luo, and Bangyu Wu

ABSTRACT

We first point out that envelope fluctuation and decay of seismic records carries ULF (ultra-low frequency, i.e. frequency below the lowest frequency in the source spectrum) signals which can be used to estimate the long-wavelength velocity structure. We then propose to use envelope inversion for the recovery of low-wavenumber components of media (smooth background) so that the initial model dependence of waveform inversion can be reduced. We derive the misfit function and the corresponding gradient operator for envelope inversion. In order to understand the long-wavelength recovery by the envelope inversion, we suggest a nonlinear seismic signal model: the "*modulation signal model*" as the basis for retrieving the ULF data and discuss the nonlinear scale separation by the envelope operator. To separate the envelope data from the wavefield data (envelope extraction), *a demodulation operator* (*envelope operator*) is applied to the waveform data. Numerical tests using synthetic data for the Marmousi model demonstrated the validity and feasibility of the proposed approach. The final results of combined EI+WI (envelope-inversion for smooth background plus waveform-inversion for high-resolution velocity structure) can deliver much improved results than the regular FWI (Full Waveform Inversion) alone. Furthermore, to test the independence of envelope to the source frequency-band, we use a low-cut source wavelet (cut from 5Hz below) to generate the synthetic data. The envelope inversion and the combined EI+WI show no appreciable difference from the full-band source results. The proposed envelope inversion is also an efficient method with very little extra work compared with conventional FWI.

INTRODUCTION

It is known that the lack of ultra low-frequency data leads to the difficulty in recovering long-wavelength background structure and therefore to the starting-model dependence of full waveform inversion (FWI) (for a review see Virieux and Operto, 2009). Traditionally, the starting model for FWI is provided by some other methods such as traveltime tomography (including ray-based or wave-based, first-arrival traveltime tomography and reflection traveltime tomography) and velocity analysis. Within FWI, long offsets, multi-scale inversion has been developed to reduce the starting model dependence (Bunks et al., 1995; Pratt et al., 1996, 1998; Sirgue and Pratt, 2004; Ravaut et al., 2004; Plessix et al., 2010, Vigh et al., 2011, Baeten et al., 2013). Multi-scale inversion is a cascade inversion starting from the lowest frequency available for the recovery of the largest scale possible. Recent development of low-frequency land source (down to 1.5 Hz) has allowed multi-scale FWI to use 1-D smooth starting model (Baeten et al., 2013). They showed that the lowest frequency band (1.5 – 2.0 Hz) is crucial in recovering the correct long-wavelength background velocity structure. However, in general, the ultra-low frequency sources are not available and the standard seismic records can go down only to about

5Hz. Therefore, starting model is still a pressing problem for FWI. Shin and Cha (2009) has performed inversion in the Laplace-Fourier domain using seismic data below 5*Hz,* to estimate the smooth, large-scale velocity structure. A recent trend is that by introducing some extra terms in the misfit functional, FWI can incorporate into its framework some other inversion methods, such as traveltime tomography or inversion (Mora, 1989; Clément et al., 2001; Xu et al., 2012; Ma and Hale, 2013; Wang et al., 2013) and velocity analysis (Biondi and Almomin, 2012, 2013; Almomin and Biondi, 2012; Tang et al., 2013).

In this paper, we extract the ULF (ultra-low frequency) signals contained in seismic trace envelopes and apply to the recovery of long-wavelength background structure without the use of low-frequency sources which are expensive or unavailable. Normalized integration method (Chauris et al., 2012; Donno et al., 2013) has used the normalized time integration of the squared waveform data as a new type of data for least-square minimization. However, much information of the envelope function has been lost due to the integration operator. We demonstrate that envelope fluctuation and decay of seismic records carries ULF signals but inaccessible from the conventional linear convolution signal model. In order to extract the envelope data from the wavefield data and keep the useful information, we need to perform a nonlinear operation using demodulation operator. For inversion we derive the gradient operator for envelope data and perform iterative inversion to obtain a smooth background model. Then we use the smooth model from envelope inversion as the starting model of waveform inversion to recover the high-wavenumber components of the model. Comparing to the linear multi-scale inversion of FWI, this is a nonlinear two-scale inversion in which the nonlinear scale separation is done by the envelope operator. The other advantage of the envelope inversion is its independence to the source wavelet. We use a low-cut source wavelet (cut from 5Hz below) to generate the synthetic data. The envelope inversion and the combined EI+WI show no appreciable difference from the full-band source results. Numerical tests using the Marmousi model demonstrated the validity and special features of the approach.

ENVELOPE INVERSION

Review of conventional FWI in the time domain

FWI (Full Waveform Inversion) can retrieve information of subsurface by fitting the difference between the recorded data d_{obs} and the simulated data d_{syn} with the proposed model. The classical least squares misfit functional is given by:

$$\begin{aligned}\sigma(\mathbf{d}) &= \frac{1}{2}\sum_{sr}\int_0^T (d_{syn}-d_{obs})^2 dt \\ &= \frac{1}{2}\sum_{sr}\int_0^T [y(t)-u(t)]^2 dt\end{aligned} \tag{1}$$

Where $u = d_{obs}$ is the observed wavefield, $y = d_{syn}$ is the synthetic wavefield. The summation is over all the sources and receivers.

The goal is to obtain the model parameter m, which can be updated as follows:

$$m_{n+1} = m_n + \alpha_n \beta_n \tag{2}$$

where α_n is the step length in the nth iteration, β_n corresponds to the updating direction which can be obtained from the gradient of the misfit function, so the gradient of the misfit function with respect to the model m must be calculated first.

Consider velocity v as the model parameter, the gradient of the misfit function with respect to v can be obtained by:

$$\frac{\partial \sigma}{\partial v} = \sum_{sr} \int_0^T [y(t) - u(t)] \frac{\partial y(t)}{\partial v} dt \tag{3}$$

Introduce an operator $\mathbf{J}$ (Jacobian) and a vector (data residual) $\boldsymbol{\eta}$, where

$$\mathbf{J} = \frac{\partial y(t)}{\partial v}, \quad \boldsymbol{\eta} = y(t) - u(t) \tag{4}$$

then equation (3) can be written as

$$\frac{\partial \sigma}{\partial v} = \mathbf{J}^T \boldsymbol{\eta} \tag{5}$$

The Jacobian $\mathbf{J}$ is also called the linear Fréchet derivative. It is known that this gradient can be calculated by zero-lag correlation of the forward propagated source wavefields and the backward propagated residual wavefields $\boldsymbol{\eta}$ (Lailly, 1983; Tarantola, 1984; Pratt et al., 1998; Pratt, 1999).

Misfit functional and gradient operator for envelope inversion

Now we define the misfit functional and derive the corresponding gradient operator for the envelope inversion. Here the "data" to be used in the misfit functional are the trace envelopes, not directly the traces (waveforms). Bozdag et al. (2011) have discussed the envelope misfit functional and its use in the kernel sensitivity analysis of global seismic tomography. However, their purpose is to use the instantaneous amplitude and phase information of individual arrivals, such as the first P or S arrivals, so they apply a short time-window to the traces for isolating the chosen arrivals. For our envelope inversion, we need to extract and treat the envelope of the whole trace.

We adopt the power objective functional to minimize the residual:

$$\begin{aligned}
\sigma(\mathbf{d}) &= \frac{1}{2} \sum_{sr} \int_0^T \left| d_{syn}^p - d_{obs}^p \right|^2 dt = \frac{1}{2} \sum_{sr} \int_0^T \left| e_{syn}^p - e_{obs}^p \right|^2 dt \\
&= \frac{1}{2} \sum_{sr} \int_0^T \left\{ \sqrt{y^2(t) + y_H^2(t)}^p - \sqrt{u^2(t) + u_H^2(t)}^p \right\}^2 dt \\
&= \frac{1}{2} \sum_{sr} \int_0^T E^2 dt
\end{aligned} \tag{6}$$

where e is the envelope function, u and y are the observed and synthetic waveforms respectively, u_H and y_H are the corresponding Hilbert transforms. "*E*" is the *instant envelope data residual* and the summation is over all the sources and receivers. p is the power for the envelope data, it can be any positive numbers. The extraction of the envelope function and the information contained in envelopes will be discussed in details in next section. The gradient operator can be derived from the partial derivative of the misfit with respect to the model perturbations as follows (for detailed derivation, see Appendix):

$$\begin{aligned}
\frac{\partial \sigma}{\partial v} &= \sum_{sr} \int_0^T E \cdot \frac{\partial \sqrt{y^2(t) + y_H^2(t)}^p}{\partial v} dt \\
&= p \cdot \sum_{sr} \int_0^T E \cdot \sqrt{y^2(t) + y_H^2(t)}^{p-2} \left[y(t) \cdot \frac{\partial y(t)}{\partial v} + y_H(t) \cdot \frac{\partial y_H(t)}{\partial v} \right] dt \\
&= p \cdot \sum_{sr} \int_0^T E \cdot e_{syn}^{p-2} \left[y(t) \cdot \frac{\partial y(t)}{\partial v} + y_H(t) \cdot \frac{\partial y_H(t)}{\partial v} \right] dt \\
&= p \cdot \sum_{sr} \int_0^T \left[E y(t) e_{syn}^{p-2} \cdot \frac{\partial y(t)}{\partial v} - H\left\{ E y_H(t) e_{syn}^{p-2} \right\} \cdot \frac{\partial y(t)}{\partial v} \right] dt \\
&= p \cdot \sum_{sr} \int_0^T \left[E y(t) e_{syn}^{p-2} - H\left\{ E y_H(t) e_{syn}^{p-2} \right\} \right] \cdot \frac{\partial y(t)}{\partial v} dt
\end{aligned} \tag{7}$$

We introduce the Fréchet derivative operator (matrix) $\mathbf{J}$ and the effective residual vector $\boldsymbol{\eta}$, defined as

$$\mathbf{J} = \frac{\partial y(t)}{\partial v}, \quad \boldsymbol{\eta} = E y(t) e_{syn}^{p-2} - H\left\{ E y_H(t) e_{syn}^{p-2} \right\} \tag{8}$$

So equation (7) can also be written as a matrix equation

$$\frac{\partial \sigma}{\partial v} = \mathbf{J}^T \boldsymbol{\eta} \tag{9}$$

This envelope inversion can also be implemented using back propagation method, and the term in the square brackets serves as the effective residual, which is the envelope residual riding on the carrier signal (modulation). Note that operator $\mathbf{J}$ includes a backpropagation operator and a virtual source operator (See Pratt et al., 1998). From the above equations, we see that the L-S (least-square) residual is calculated using envelope data, but the backprojection of the envelope residual to the model space is done by backpropagation using the carrying signal with the envelope residual riding on its shoulder. Based on the above equations, envelope inversion algorithm can be developed following the algorithm of time-domain waveform inversion.

To see the effect of the parameter p, we rewrite the misfit function in equation (6) as follow:

$$\begin{aligned}\sigma(\mathbf{d}) &= \frac{1}{2}\sum_{sr}\int_0^T \left[e_{syn}^p - e_{obs}^p\right]^2 (t)dt \\ &= \frac{1}{2}\sum_{sr}\int_0^W \left[e_{syn}^p - e_{obs}^p\right]^2 (\omega)d\omega \\ &= \frac{1}{2}\sum_{sr}\int_0^W \left[e_{syn}^p(\omega) - e_{obs}^p(\omega)\right]^2 d\omega\end{aligned} \tag{10}$$

Calculate the gradient operator, we get:

$$\frac{\partial\sigma}{\partial v} = \sum_{sr}\int_0^W \left[e_{syn}^p(\omega) - e_{obs}^p(\omega)\right]\cdot\frac{\partial e_{syn}^p(\omega)}{\partial v}d\omega \tag{11}$$

Since e_{syn} is a function with respect with y and y_H, using the chain rule we know that the above equation can be written in the following form:

$$\frac{\partial\sigma}{\partial v} = \sum_{sr}\int_0^W \left[e_{syn}^p(\omega) - e_{obs}^p(\omega)\right]\cdot\left\{\frac{\partial e_{syn}^p(\omega)}{\partial y}\frac{\partial y}{\partial v} + \frac{\partial e_{syn}^p(\omega)}{\partial y_H}\frac{\partial y_H}{\partial v}\right\}d\omega \tag{12}$$

Figure 1 shows two traces generated from the Marmousi model. The top panel are the original traces; the middle panel are trace envelope in the time domain with different value of p (the amplitudes have been normalized); the bottom panel are the trace envelope in the frequency domain with different value of p (the amplitudes have been normalized). We see that different values of power p of envelope data have the effect of preconditioning the data in both the time and frequency domains. In the time domain higher power p put heavier weight on the energetic arrivals, in this case (acoustic wave) earlier envelope arrivals, especially the direct arrivals (including turning waves); while in the frequency domain, heavier weight on the low-frequency envelope data. We tested three cases, p = 1, 2, 3. The parameter p = 3 diminish the later arrivals too much and the inversion cannot penetrate to the depth. Therefore, in applications we use only p = 1, 2. In next section, we show that p = 2 is a good choice for the Marmousi data set, which provides a good balance on windowing the data for stable inversion to recover the long-wavelength background velocity structure.

INFORMATION IN THE ENVELOPE AND THE MODULATION SIGNAL MODEL

Envelope operator (demodulation operator)

In equation 6 we have introduced the envelope function for the misfit functional. The envelope function is extracted from the waveform data by an ***envelope operator*** (or ***demodulation operator***). The ***envelope operator*** $\mathcal{E}\left[f(t)\right]$ is consisted of two steps:

(1) *Analytic transform of trace* $f(t)$

$$f_a(t) = f(t) + iH(f)(t) = f(t) + if_H(t) \tag{13}$$

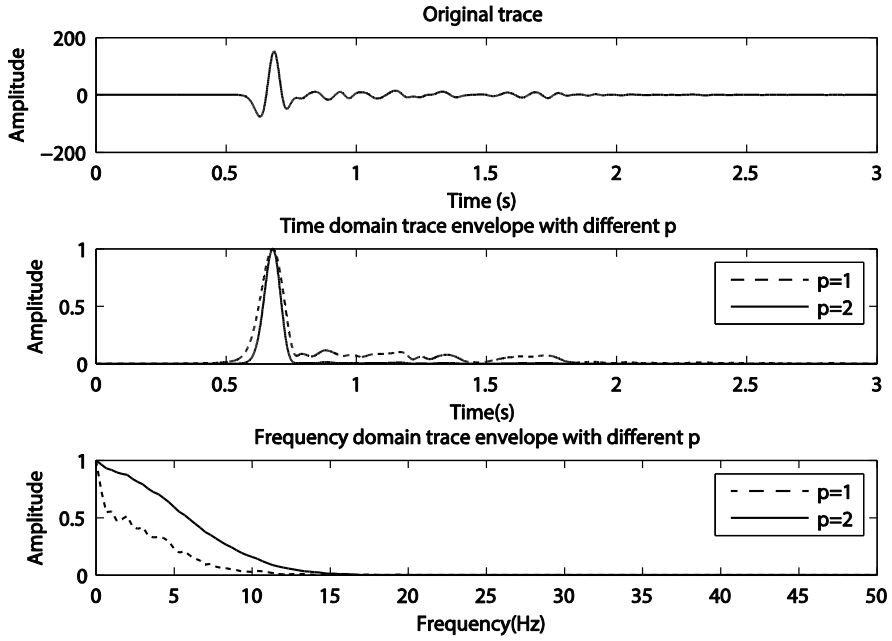

(a)

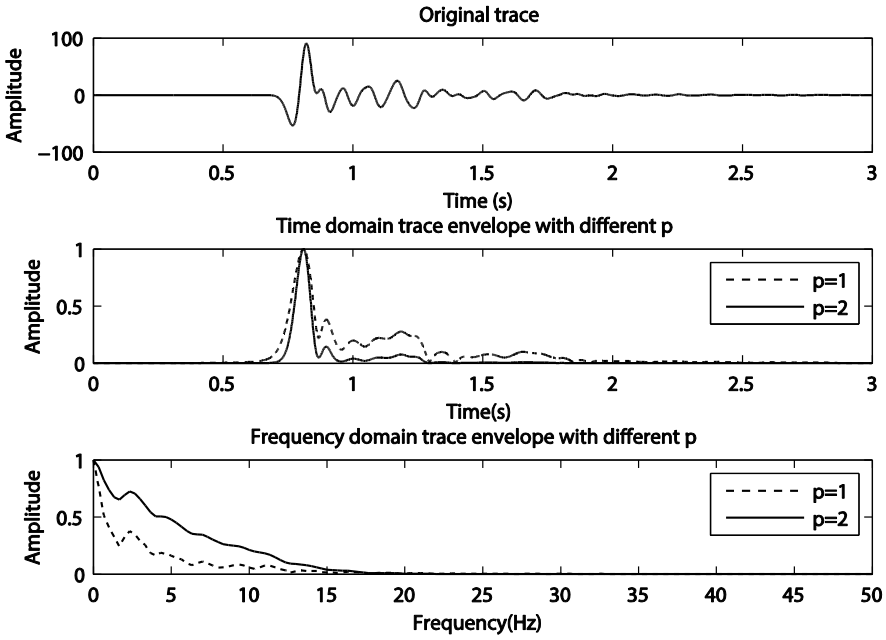

(b)

Figure 1 Data traces generated from Marmousi model and their envelopes with different powers (different values of p) in both the time domain and frequency domain.

where $H(f)(t)$ is the Hilbert transform of a real function *f*, and f_a is the analytic signal (complex) corresponding to *f*.

(2) *Take magnitude of the analytic signal*

$$\begin{aligned} \mathcal{E}_f^2(t) &= \mathcal{E}^2[f(t)] = |f_a(t)|^2 = \mathrm{Re}(f_a(t)]^2 + [\mathrm{Im}(f_a(t)]^2 = f(t)^2 + f_H(t)^2 \\ \mathcal{E}_f(t) &= sqrt\{\mathcal{E}_f^2(t)\} \end{aligned} \tag{14}$$

Now we discuss the properties of the envelope operator and information contained in envelopes.

Since envelope operator contains a square-root operator, it is a nonlinear operator (nonlinear filtering). From the modulation theory in signal processing (e.g. Robinson et al., 1986), we see that the envelope operator is equivalent to a demodulation operator if we consider a seismogram as a modulated signal: the low-frequency envelope is the modulation signal and the high-frequency reflection waveforms as the carrier signal. We will discuss the signal model in the next subsection. But let us know concentrate on the properties of the extracted envelopes. From the modulation theory we know that amplitude modulation is a nonlinear operation, and the modulation frequency is riding on the shoulders of the carrying frequency, as show schematically in Figure 2. Although the modulation frequency may be very low, it does not show up in the corresponding low frequency range in the frequency-domain representation of the modulated signal. In this Figure, (a) is the modulation signal (the envelope); the carrier signal is a sinusoidal signal with a carrier frequency of 8Hz, (b) is the modulated signal which is the product of the modulation signal and the carrier signal; (c) and (d) is the spectra of the modulation signal and the modulated signal respectively (the amplitudes have been normalized). Only the nonlinear demodulation operator can extract the low-frequency information coded in the envelope.

Figure 3(a) shows a shot profile of waveform data (top) and envelope data (bottom) from the synthetic data set of the Marmousi model (see next section); The corresponding waveform spectra (top) and envelope spectra (bottom) are plot in Figure 3(b). We clearly see that the envelope data have ULF spectra compared with the waveform data. From Figure 1 and 3, we can also see that envelope shapes are different for different parts of the traces. For the early arrivals of near offsets, the envelopes look like individual envelopes of the source wavelet; however, for later arrivals and even early arrivals of far offsets, the envelopes become continuous fluctuations due to the interference between many arrivals and the nonlinearity of the envelope operator. The match of envelope data residual may avoid the high-frequency cycle skipping, reduce local minima and decrease the sensitivity to high-frequency noises.

Modulation signal model

In order to better understand the nonlinear nature of the envelope operator and its effects on information extraction from seismograms, we first discuss the modulation signal model for surface reflection seismic data.

In surface reflection survey, the data set (wavefield records) is composed of direct arrivals (including turning waves) and scattered waves from subsurface reflectors. For the formation of

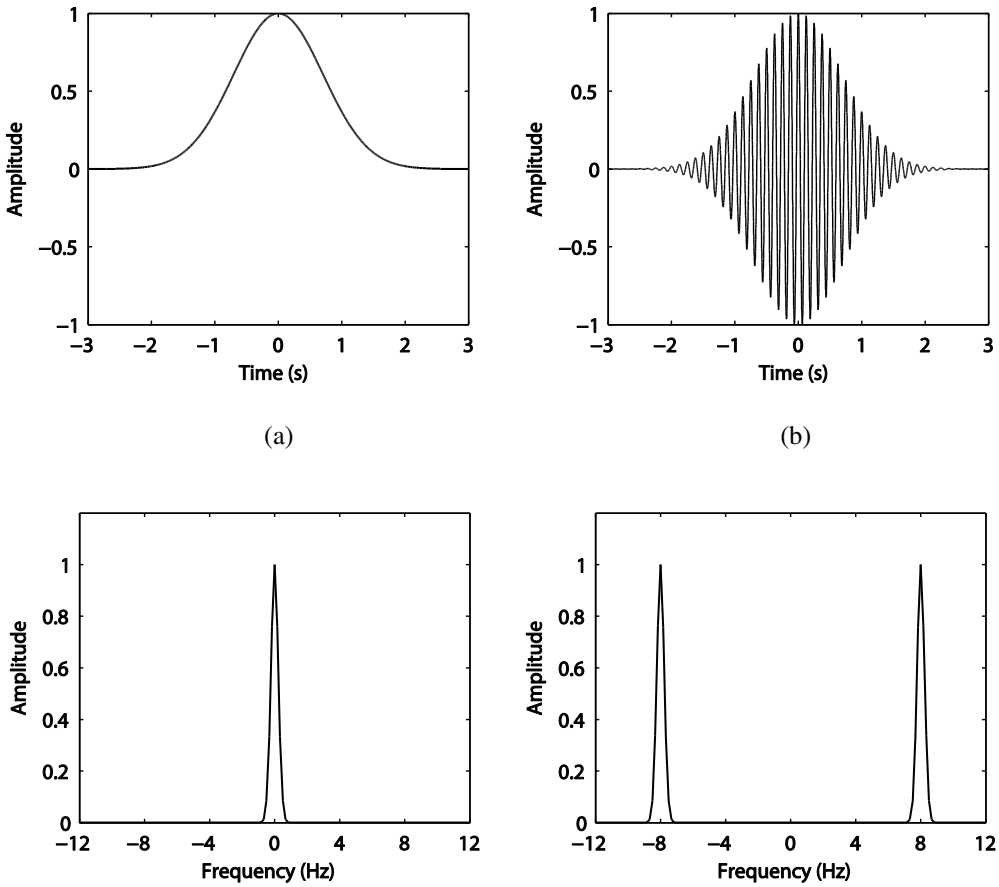

Figure 2 (a) The modulation signal; (b) the modulated signal; (c) the spectra of the modulation signal (with a carrier frequency of 8Hz); (d) the spectra of the modulated signal.

reflection data, the roles of forward scattering and backscattering are very different from each other. Forward scattering only modifies the Green's function (propagator) of the background medium (smooth part), while backscattering of reflectors is actually responsible for the generation of reflection signals.

In the frequency domain the wave field measured on the surface can be modeled as:

$$p(\omega,\mathbf{x}_r,\mathbf{x}_s)=p^0(\omega,\mathbf{x}_r,\mathbf{x}_s)+p^{sc}(\omega,\mathbf{x}_r,\mathbf{x}_s) \tag{15}$$

where $p^0(\omega,\mathbf{x}_r,\mathbf{x}_s)=g(\omega,\mathbf{x}_r,\mathbf{x}_s)$ is the direct wavefield in the background medium (including turning waves), and $p^{sc}(\mathbf{x}_r,\mathbf{x}_s)$ is scattered field received by geophone at $\mathbf{x}_r$ due to a source at $\mathbf{x}_s$.

Now we discuss the seismograms formed by backscattered waves, which can be modeled as:

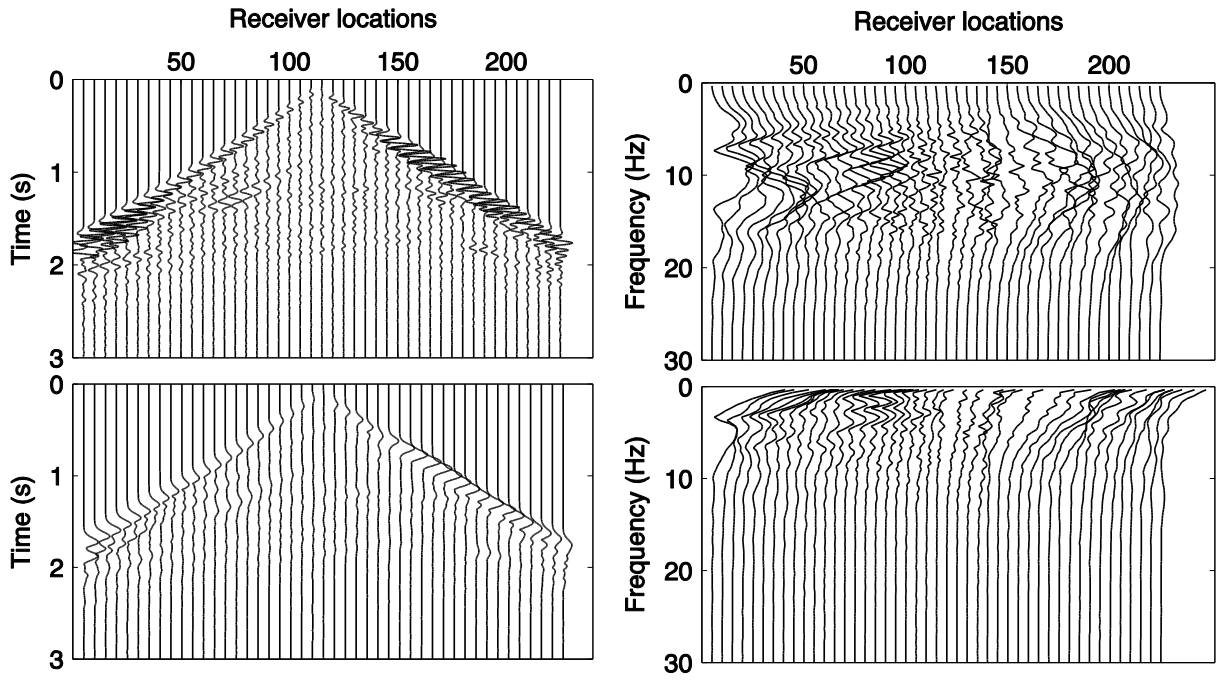

(a) (b)

Figure 3 (a) A shot profile of waveform data (top) and envelope data (bottom); (b) waveform spectra (top) and envelope spectra (bottom). The data are from the synthetic data set of the Marmousi model.

$$p^{bsc}\left(\omega,\mathbf{x}_r,\mathbf{x}_s\right)=s(\omega)\int_S g_M\left(\mathbf{x},\mathbf{x}_s\right)g_M\left(\mathbf{x}_r,\mathbf{x}\right)\gamma\left(\mathbf{x}\right)dS(\mathbf{x}) \tag{16}$$

where S represents all the reflection surfaces in the model space, g_M is the modeling Green's function which is a full-wave Green's function, $s(\omega)$ is the source spectrum and $\gamma\left(\mathbf{x}\right)$ is scattering coefficient of the reflector element. The full-wave Green's function can be decomposed into a primary-wave part and a multiple-wave part:

$$g_M = g_F + g_{mul} \tag{17}$$

where g_F is the forward-scattering Green's function, which includes all the forward-scattering effects (the transmission mode), such as refraction, diffraction, geometric spreading and focusing effects and therefore contains the average velocity information along the propagation path; while g_{mul} contains multiply scattered waves from other scatterers. To simplify the treatment, we consider only the primary reflections, so g_{mul} is neglected. The approximation is similar to the De Wolf approximation (De Wolf, 1971, 1985; Wu, 1994, 2003). We know that the scattering models for forward-scattering and backscattering are very different, and therefore the information contained in the reflection series $\gamma\left(\mathbf{x}\right)$ and in the forward scattering approximated

Green's function g_F represents different properties of medium perturbations. In the case of direct arrivals, g_F contains velocity perturbations along the propagation path; while for reflected arrivals, $\gamma(\mathbf{x})$ corresponds to local reflectivity due to impedance jump (velocity jump for acoustic media with constant density).

Assuming there are totally L's interfaces (including reflector surfaces) and each interface has M_l elements (after discretization), so the total number of scattering elements is $N = \sum_{l=1}^{L} M_l$. Then the primary backscattered field (discretized version of (16)) can be modeled as reflection series

$$p^{bsc}(\omega, \mathbf{x}_r, \mathbf{x}_s) = s(\omega) \sum_{i=1}^{N} g_F(\omega, \mathbf{x}_i, \mathbf{x}_s)\, g_F(\omega, \mathbf{x}_r, \mathbf{x}_i)\, \gamma(\mathbf{x}_i)\, ds(\mathbf{x}_i) \tag{18}$$

For simplicity, we take the reflection coefficients as frequency-independent. The frequency-domain and time-domain solutions for reflected signals can be written as:

$$\begin{aligned} p^{bsc}(\omega, \mathbf{x}_r, \mathbf{x}_s) &= s(\omega) \sum_i g_F(\omega, \mathbf{x}_i, \mathbf{x}_s)\, g_F(\omega, \mathbf{x}_r, \mathbf{x}_i)\, \gamma(\mathbf{x}_i) \\ p^{bsc}(t, \mathbf{x}_r, \mathbf{x}_s) &= s(t) * \sum_i g_F(t, \mathbf{x}_i, \mathbf{x}_s) * g_F(t, \mathbf{x}_r, \mathbf{x}_i)\, \gamma(\mathbf{x}_i) \end{aligned} \tag{19}$$

where "*" denotes time convolution. Green's functions can be expressed in a form

$$\begin{aligned} g_F(\omega, \mathbf{x}_i, \mathbf{x}_s) &= |g_s(\omega)|(\mathbf{x}_i)\, exp[-i\omega\tau_s(\mathbf{x}_i)] \\ g_F(\omega, \mathbf{x}_i, \mathbf{x}_r) &= |g_r(\omega)|(\mathbf{x}_i)\, exp[-i\omega\tau_r(\mathbf{x}_i)] \end{aligned} \tag{20}$$

where τ_s and τ_r are the corresponding time-delays due forward-scattering along the source path and receiver path, respectively. We define a propagator

$$G_{sr}(\omega, \mathbf{x}_i; \mathbf{x}_s, \mathbf{x}_r) = |g_s(\omega)||g_r(\omega)| exp\{-i\omega[\tau_s(\mathbf{x}_i) + \tau_r(\mathbf{x}_i)]\} \tag{21}$$

so the reflection seismograms can be modeled as reflection time series

$$\begin{aligned} p^{bsc}(t, \mathbf{x}_r, \mathbf{x}_s) &= \sum_i R_w(\mathbf{x}_r, \mathbf{x}_s; t - \tau_i) = s(t) * \sum_i G_{sr}(t, \mathbf{x}_i; \mathbf{x}_s, \mathbf{x}_r)\, \gamma(t, \mathbf{x}_i) \\ \gamma(t, \mathbf{x}_i) &= \gamma_i \delta(t - \tau_i) \end{aligned} \tag{22}$$

Here the spatial distribution of reflectors in the 3-D space is transformed into a time series by a distance-time correspondence in a background medium (e.g. homogeneous medium). The above equation is the traditional *convolution signal model* (Robinson, 1957; Robinson et al., 1986), in which the propagator (Green's function pairs) $G_{sr}(t, \mathbf{x}_i; \mathbf{x}_s, \mathbf{x}_r)$ only modify the travel-times and amplitudes of the reflection events, and the signal spectrum is mainly determined by the source wavelet. Both the amplitude and phase functions of the propagator G_{sr} are smoothly varying

functions. The neglect of g_{mul} is equivalent to the drop of "reverberation waveform" in the convolution model (Robinson et al., 1986). We see that the propagator, although carrying smooth medium information, can only modify the source spectrum. Based on the linear signal model, we are restricted to only access the information provided within source spectra. This convolution model is good for seismic imaging, since it provides the mathematical model for resolution analysis and resolution enhancement (such as deconvolution) in high-resolution imaging. However, depending on the information you want to extract from the seismic records (seismograms), one can define different signal models. In fact, seismograms have much rich information than the convolution model predicts. For seismic inversion, we need the low-frequency information contained in seismograms for the recovery of long-wavelength background velocity structure. We see from the above analysis that there is low-frequency information coded into the envelope fluctuation and decay of seismograms, but not accessible from linear convolution model. The problem is how to take use of the information associated with g_F coded in the envelope for the estimate of long-wavelength velocity structure in waveform inversion. Demodulation operator can peel off the envelope from the seismograms, and therefore can in certain way decode the low-frequency information not reachable by linear methods. To understand the demodulation operator and its effect to the signal spectra, we need to consider the modulation signal theory.

We reformulate and redefine the signal model of equation (18) as a ***modulation model***. Since the propagator $G_{sr}(t,\mathbf{x}_i;\mathbf{x}_s,\mathbf{x}_r)$ is a smooth function of time with respect to the reflection series, so the signal model (18) can be rewritten as:

$$\begin{aligned} p^{bsc}(t,\mathbf{x}_r,\mathbf{x}_s) &= \sum_i G_{sr}(t;\mathbf{x}_s,\mathbf{x}_r)\gamma_i(t,\mathbf{x}_i) * s(t) \\ &\simeq G_{sr}(t;\mathbf{x}_s,\mathbf{x}_r)\gamma_w(t) \\ \gamma_w(t) &= \sum_i s(t) * \gamma_i(t,\mathbf{x}_i) \end{aligned} \tag{23}$$

where $\gamma_w(t)$ is the reflectivity series with the source wavelet signature, which is considered as the carrier signal, while G_{sr} is the modulation signal. The high-frequency carrier signal is modulated by the earth medium though wave propagation (only forward-scattering involved). We can consider the reflection series (23) as a *Modulation-convolution signal model*, or simply as a ***modulation signal model*** for the reflection series if we are concern mainly on the low-wavenumber background recovery (This signal model has been briefly discussed in Wu et al., 2012, 2013). In fact we can say that the carrier and the modulation signals contain quite different information about the earth media. The carrier $\gamma_w(t)$ is formed by impedance discontinuities convolved with the source wavelet; while the modulator G_{sr} contains mainly the information on the smoothed medium velocity structure (under the forward-scattering approximation).

Now we include the direct arrivals, which can be written as:

$$\begin{aligned} p^d(\omega,\mathbf{x}_r,\mathbf{x}_s) &= p^0(\omega,\mathbf{x}_r,\mathbf{x}_s) + p^{dsc}(\omega,\mathbf{x}_r,\mathbf{x}_s) \\ p^d(t,\mathbf{x}_r,\mathbf{x}_s) &= g^d(t,\mathbf{x}_r,\mathbf{x}_s) * s(t) \end{aligned} \tag{24}$$

where

$$g^d(t,\mathbf{x}_r,\mathbf{x}_s)=\int d\omega e^{-i\omega t}g^d(\omega,\mathbf{x}_r,\mathbf{x}_s) \tag{25}$$

is the Green's function for the direct arrival and is assumed to be a much slower time-varying function than the source wavelet. Since the direct arrivals are single arrivals or sparse arrivals, so the convolution can be approximated by product. Including the direct arrivals (24) and the reflection series (23), the modulation signal model for the whole seismogram can be expressed as:

$$p\left(t,\mathbf{x}_r,\mathbf{x}_s\right)=g^d(t,\mathbf{x}_r,\mathbf{x}_s)s(t)+G_{sr}\left(t;\mathbf{x}_s,\mathbf{x}_r\right)\gamma_w\left(t\right) \tag{26}$$

For a seismogram including the reflection series, we can view it as a product of two functions: a carrier signal and a modulator. For the direct arrivals, the carrier is the source wavelet, and the modulator is the direct propagator (Green's function); for the reflect series, the carrier is $\gamma_w\left(t\right)$ and the modulator is the propagator $G_{sr}\left(t;\mathbf{x}_s,\mathbf{x}_r\right)$. If we apply a long-wavelength velocity perturbation to a given model, but keep the impedance jumps unchanged, then the propagator will change, resulting in a modulation in both amplitude and phase to the original reflection series. After demodulating the traces, the envelope changes (residuals) contain the long-wavelength information of the velocity perturbation. This provides the signal basis for long-wavelength background recovery.

Now we look at the consequence and effect of demodulation operator applied to the modulation model (equation (26)). We apply the Hilbert transform product theorem, i.e. the Bedrosian-Brown theorem (Bedrosian, 1962; Brown, 1986), to the trace model (26),

$$\begin{aligned} H\left\{p\left(t,\mathbf{x}_r,\mathbf{x}_s\right)\right\} &= H\left\{g^d(t,\mathbf{x}_r,\mathbf{x}_s)s(t)+G_{sr}\left(t;\mathbf{x}_s,\mathbf{x}_r\right)\gamma_w\left(t\right)\right\} \\ &= g^d(t,\mathbf{x}_r,\mathbf{x}_s)H\left\{s(t)\right\}+G_{sr}\left(t;\mathbf{x}_s,\mathbf{x}_r\right)H\left\{\gamma_w\left(t\right)\right\} \end{aligned} \tag{27}$$

Since the propagator functions $g^d(t,\mathbf{x}_r,\mathbf{x}_s)$ and $G_{sr}\left(t;\mathbf{x}_s,\mathbf{x}_r\right)$ are low-pass functions (slowly varying function) (under the forward-scattering approximation) and satisfies the Brown's condition for demodulation (ibid), so it can be pulled out of the Hilbert transform. Therefore, the envelope function of the seismic traces can be approximated by

$$\begin{aligned} \mathcal{E}^2(t) &= \left|p_a(t)\right|^2 = p^2(t)+p_H^2(t) \\ &\doteq \left(g^d(t)\right)^2\left[s^2(t)+s_H^2(t)\right]+G_{sr}^2\left(t\right)\left[\gamma_w^2\left(t\right)+\left(H\left\{\gamma_w\left(t\right)\right\}\right)^2\right] \\ &= \left(g^d(t)\right)^2\mathcal{E}^2\left[s(t)\right]+G_{sr}^2\left(t\right)\mathcal{E}^2\left[\gamma_w(t)\right] \end{aligned} \tag{28}$$

where $\mathcal{E}^2\left[s(t)\right]$ is the squared envelope of the source wavelet. In deriving the above equation, we neglected the cross-talk between the direct arrival energy and the reflection series energy. This assumption is valid for near and medium offsets due to the travel-time difference. For far offsets, the approximation may not be valid and needs further study. However, this approximation is not critical for envelope extraction. We see that taking envelope of seismograms (demodulation) is

equivalent to the application of a nonlinear signal filtering, resulting in the extraction of low-frequency information coded in the seismograms. For direct arrivals (the first term in the right-hand side), the resulted envelope-gram (envelogram) has the effect of using a low-resolution wavelet (a Gaussian pulse) to replace the original high-frequency wavelet (Ricker wavelet). For reflection series (The second term in the right-hand-side), $\mathcal{E}^2\left[\gamma_w(t)\right]$ will extract only the low-frequency part of the carrier signal $\gamma_w(t)$. We also noticed that the envelope operator keeps the long-wavelength information riding on the propagator G_{sr} untouched. In this way, the high-wavenumber reflection information is peeled off and only low-wavenumber background is kept in the envelograms.

Nonlinear scale separation by envelope operator

It is well-known that seismic data has a *wavenumber gap* (or a *scale gap*) in terms of subsurface structure inversion. That is the lack of intermediate wavenumber (medium-scale) information about the subsurface media in the data (Claerbout 1983; Jannane *et al*. 1989; Mora, 1989; Ghosh 2000; Latimer *et al*. 2000; Plessix et al., 2012; Baeten et al., 2013). For 3-D earth structure, this gap is the combined results of limited acquisition frequency-band and limited observation aperture. For surface reflection survey with limited acquisition aperture, the gap is mainly caused by the lack of low-frequencies in source spectra (e.g., Latimer et al., 2000; Baeten et al., 2013). Therefore, substantial efforts have been paid to develop low-frequency sources. Big gun arrays and a deeper towing depth can provide low frequencies down to as low as 2Hz, but even lower frequencies are still needed (Vigh et al, 2011; Baeten et al., 2013). Recently, low-frequency land source (vibrator with nonlinear frequency sweep) has been reported (Plessix et al., 2012; Baeten et al., 2013) which can extent the low-frequency end to 1.5 Hz. FWI using the corresponding data showed improved low-wavenumber background recovery. Due to the availability of low-frequency data, they could use a 1-D smooth starting model in their multi-scale inversion scheme. They showed that the lowest frequency band (1.5 – 2.0 Hz) is crucial in recovering the correct low-wavenumber background velocity structure.

As we mentioned above, the linear scale separation is usually realized by a multi-scale inversion: the large-scale recovery is done using the low-frequency data and the smaller scales are recovered from the high-frequency data subsequently. In this linear approach, the expensive low-frequency source is a necessary and critical armament for success. In the following we discuss the *nonlinear scale separation* through envelope operator.

To simplify the scale analysis, in the following we mainly discuss the scale response for vertical structural variations as in previous discussions (Jannane et al., 1989; Baeten et al., 2013). From equation (28) and Figure 2-3, we see that the envelope operator can peel off the low-frequency envelope from the waveform traces. The low-frequency nonlinear extraction in fact separates the large-scale response which is coded in the envelope, from the waveform data which are the band-limited response to the medium perturbation. This is very different from the concept of linear scale separation which depends on the linear correspondence between the signal frequency and medium scale. In Figure 4a we show the comparison of waveform spectrum (blue line) and envelope spectrum (red line) for the Marmousi data with a full Ricker source excitation. In the figure we also plot the average medium velocity spectrum (thin grey line) and the average

velocity perturbation (medium velocity subtracts the background velocity) spectrum (dotted line). In order to see the correspondence of medium wavenumber spectra to the data frequency spectra, we perform a z-t transform using the known velocity structure. The medium spectrum shown on the figure is the average over all the vertical profiles. The same has done for the perturbation spectrum. Form Figure 4a, we see that for the waveform data, the low-frequency spectral components are missing so the long-wavelength part of the perturbation spectrum is not covered. Compared with envelope spectrum, we see the complimentary role of envelope data which has strong low-frequency components but has very weak high-frequency components. This property of the envelope function can reduce the cycle skipping and local minima problems of waveform data and can recover the long-wavelength components of the perturbation structure as show in the next section for the Marmousi model. Of course its limitation needs to be further studied.

Because of the nonlinear nature of the envelope operator, the low-frequency contents of the envelope data do not tightly depend on the source spectrum, which is a sharp contrast to the conventional FWI. In Figure 4b we plot a similar spectral comparison as in Figure 4a, but using a low-cut Ricker source. When generating synthetic seismograms, the source wavelet was filtered with a 5 Hz low-cut taper. From the spectrum of waveform data thus generated, we see very little energy exists below 5 Hz. Later in the FWI tests we can see much worse results than the full-band source because of the lack of low-frequency energy. However, the spectrum of the envelope data (average over all the traces) does not show too much difference from the full-band source case. This demonstrates the nonlinear nature of the envelope extraction, which does not have the linear correspondence between the source spectrum and the data spectrum. Later in the inversion test section, we will show that the inversion results for these two cases are very similar, showing the independence of envelope inversion to the source spectra.

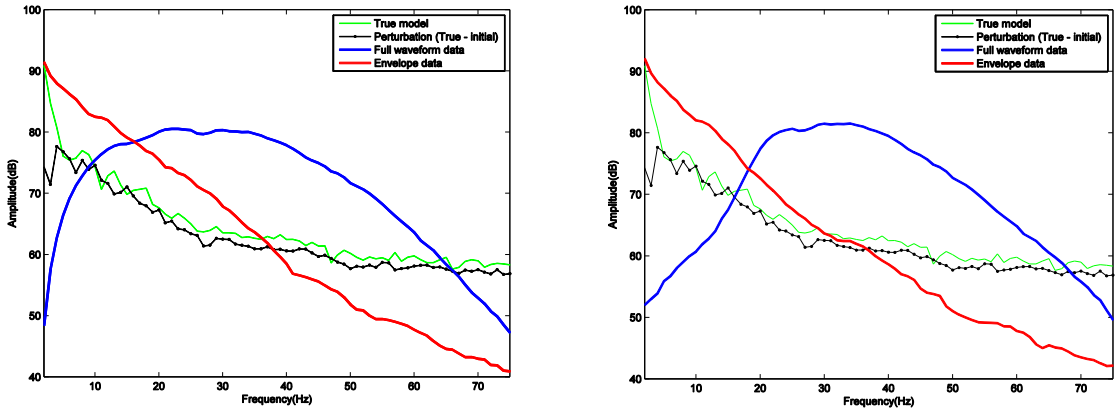

(a) (b)

Figure 4 (a) Comparison of waveform spectrum and envelope spectrum for the Marmousi data with a full Ricker source excitation; (b) Same as (a) but with a low-cut source excitation. The low-cut source is obtained by a 5Hz low-frequency taper.

This kind of nonlinear scale separation is similar to the Laplace domain inversion (Shin and Ha, 2008) and the normalized integration method (Chauris et al., 2012; Donno et al., 2013). For

linear scale separation in the multi-scale inversion method, the inversion theory is based on the Born modeling. However, for nonlinear scale separation, the forward modeling theory for the long-wavelength part is not the Born modeling. The forward modeling theory for envelope inversion needs further investigation, which may provide more insight on the benefit and limitation of the envelope inversion.

INVERSION TESTS WITH THE MARMOUSI MODEL

The data were generated by a FD algorithm with an acquisition system composed of 50 shots evenly distributed along the surface. We used total 228 receivers across the surface for each shot. The true model is shown in Figure 5(a). A linear gradient model is used as the initial model (Figure 5(b)).

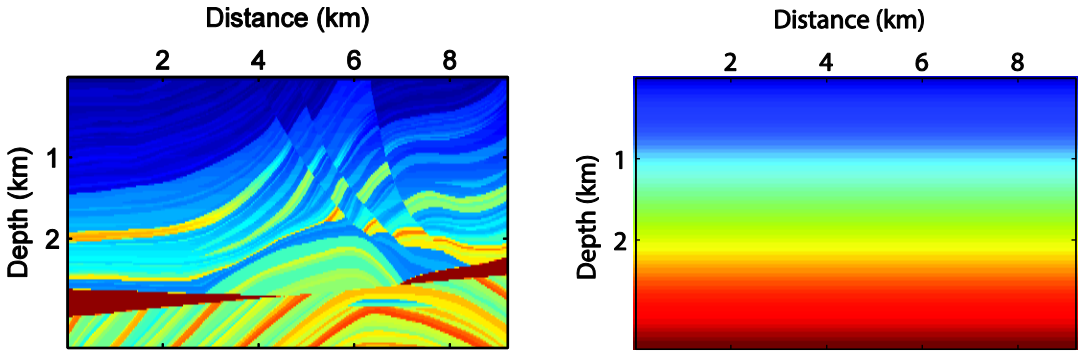

(a) (b)

Figure 5 (a) True Marmousi model; (b) linear gradient initial model.

To test the independence of envelope inversion to source spectra, especially the existence of low-frequency in the source wavelet, we use two types of ricker wavelets as the source wavelet: one is the full-band wavelet, the other is the low-cut wavelet. Figure 6 shows the two types of ricker wavelet and their envelopes in both the time domain and frequency domain. Figure 7 shows two traces selected from the data generated from the Marmousi model when using the low-cut source wavelet in Figure 6. The upper panels are the time domain traces and their envelopes, and the lower panels are the corresponding frequency domain spectra. We can see the rich low frequency information in the envelopes.

Starting from the linear initial model, the smooth backgrounds obtained from envelope inversion (after 10 iterations) are shown in Figure 8(a) and (b) for the two types of sources, respectively. We see the strong similarity of these two recovered background structures. This shows the insensitivity of EI (envelope-inversion) to the source frequency band, and further demonstrates that the long-wavelength recovery of background is from the demodulated envelope curve, not from the low-frequency source excitation. Figure 8(c) and (d) show the final results of combined inversion (EI+WI) by waveform inversion using the recovered smooth background by EI. This

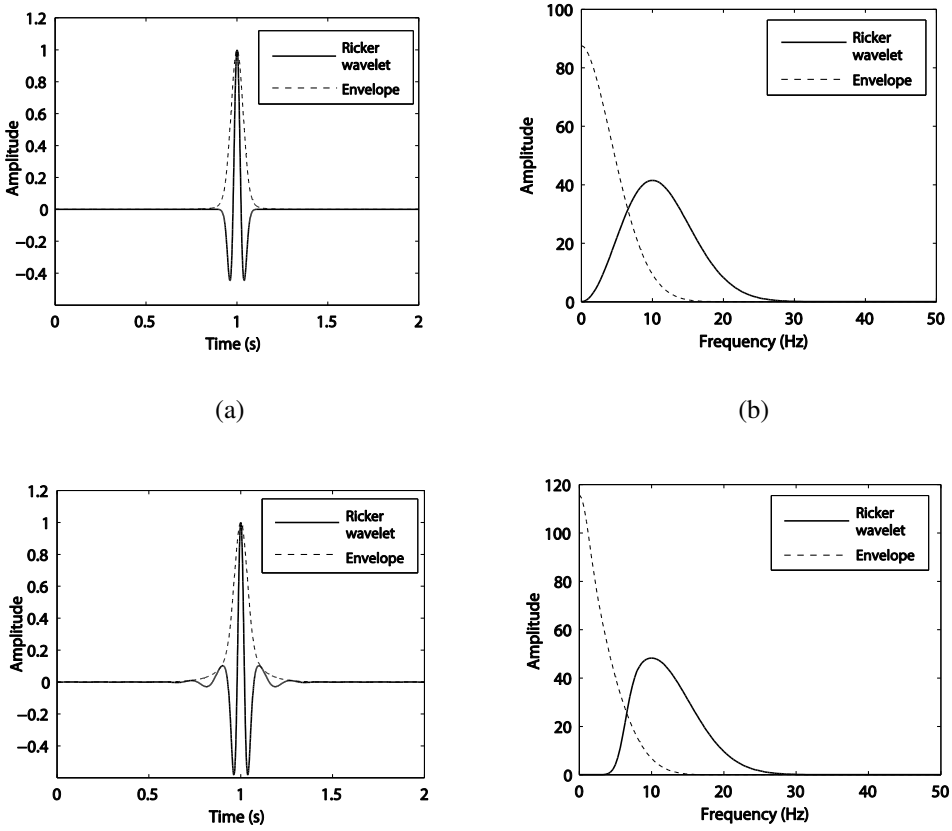

Figure 6 Ricker source wavelet (solid line) and its envelope (dashed line): (a) full-band source in time domain; (b) full-band source in frequency domain; (c) low-cut source in time domain; (d) low-cut source in frequency domain.

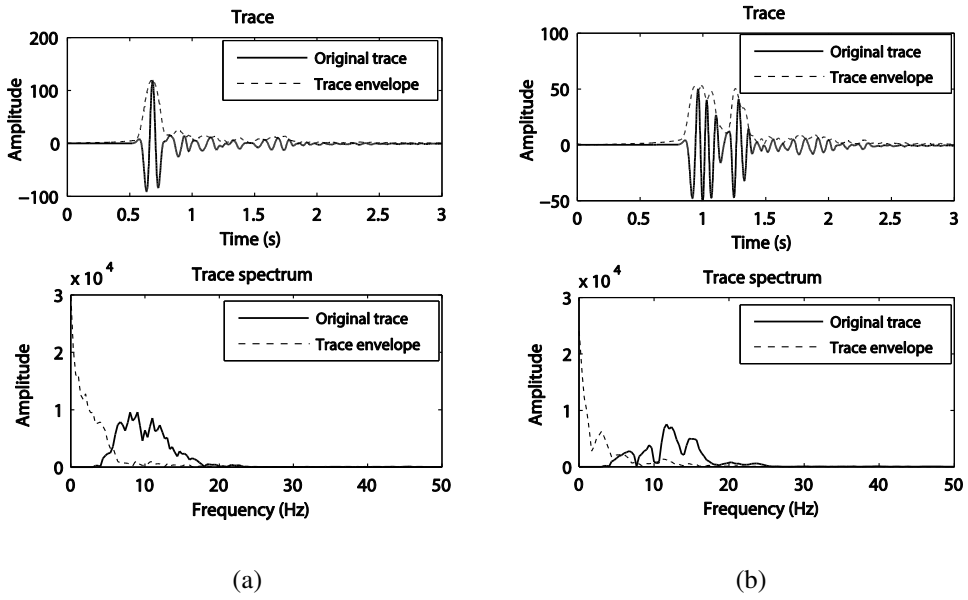

Figure 7 Two traces selected from the data generated from the Marmousi model using the low-cut Ricker wavelet. The upper panels are the time domain traces and their envelopes, and the lower panels are the corresponding spectra in the frequency domain.

strategy is similar to that used in the combined inversion of Chauris et al. (2012) and Donna et al. (2013), where they used the estimated background velocity model from the normalized integration method as the starting model for the high-wavenumber recovery by FWI. For comparison, in Figure 8(e) and (f) we show the conventional full waveform inversion results directly starting from the linear initial model. We see the significant improvement in inversion fidelity by combined inversion EI+WI. This is mainly due to the scale separation of the envelope operator, so that the long-wavelength background can be recovered correctly by EI. From Figure 8(e) and (f) we see also that conventional FWI is sensitive to the source frequency band. The inversion result using the low-cut source is noticeably worse than that of the full-band source; while the corresponding two results by EI+WI show no appreciable difference.

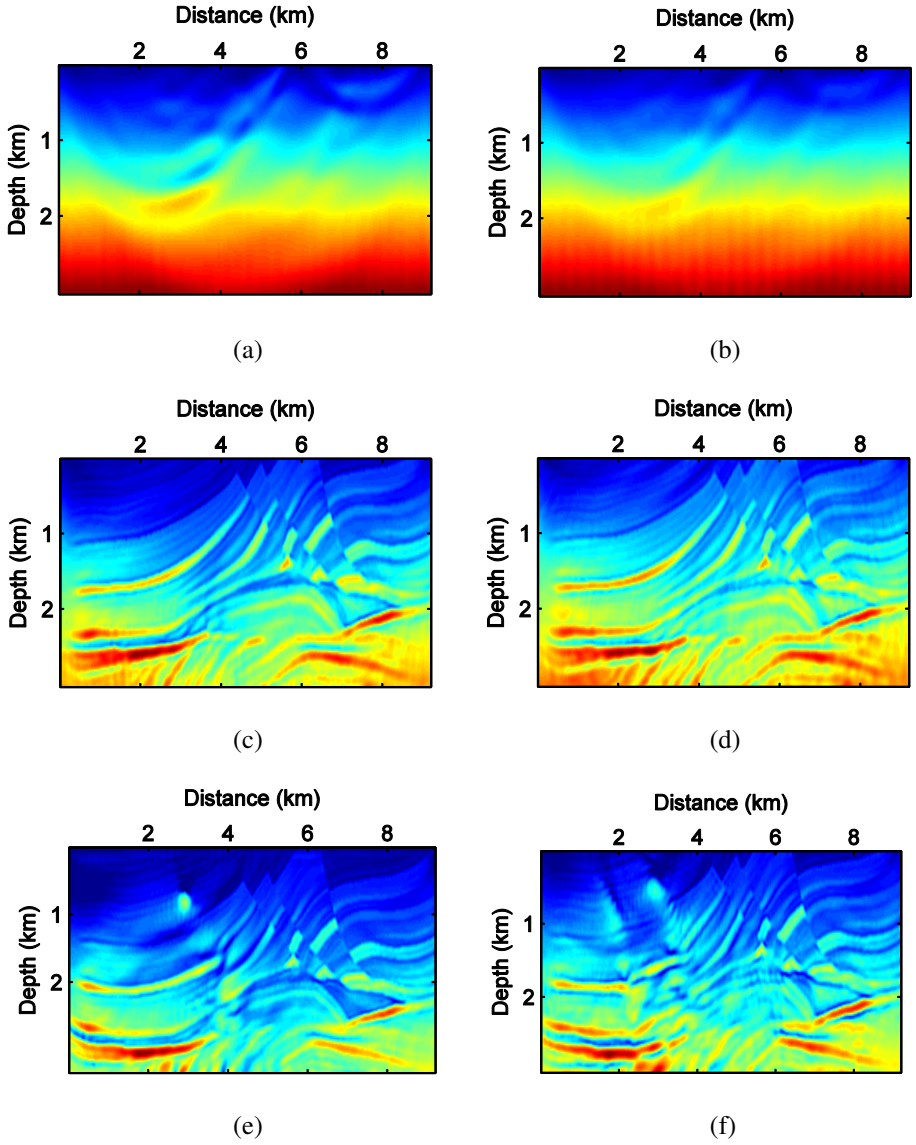

Figure 8 Envelope inversion tests on the Marmousi model: (a) Smooth background obtained from envelope inversion (EI) using the full-band source; (b) Same as (a) but with the low-cut source; (c) Combined EI+WI inversion result (waveform inversion using the smooth background from envelope-inversion) using the full-band source; (d) Combined EI+WI inversion result using the low-cut source; (e) Direct waveform inversion (FWI) from the linear initial model using the full-band source; (f) Same as (e) but using the low-cut source.

Figure 9 shows the reduction of L-S residuals with iterations. Compared with FWI (dashed line), the convergence of EI+WI (solid line) is faster and has avoided the false local minima.

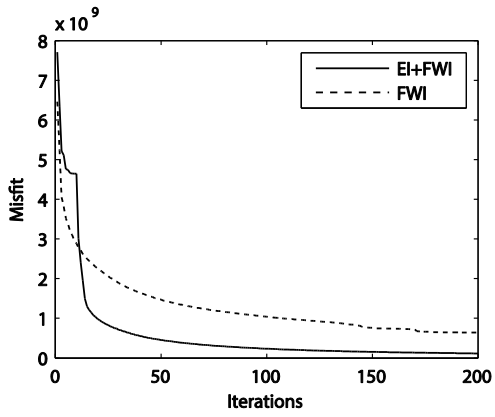

Figure 9 Reduction of L-S residuals with iterations. Comparison of EI+WI (solid line) and FWI (dashed line).

To demonstrate the effect of data power p to the result of envelope inversion, in Figure 10 we show the result of envelope inversion (EI) with $p=1$ and the final result of EI+WI. As we discussed in the previous section, the EI results in this case are much rougher than the case of $p=2$ due to the heavier weight on the later arrivals (reflections) and on the high-frequency components of the envelope data. We know that the backpropagation of envelope data is similar to energy-pact imaging, so there is no destructive interference, resulting in a noisier image than the FWI image. Note that even though the EI results of $p=1$ are very different from that of $p=2$, the final result of EI+WI in this case is very similar to the case of $p=2$. This indicates that long-wavelength background media recovered in these two cases are fairly close to each other.

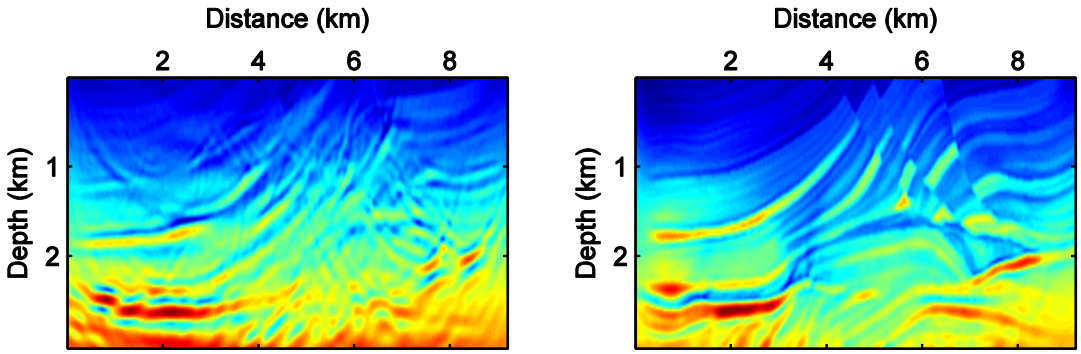

(a) (b)

Figure 10 Envelope inversions (EI) with $p=1$ (a). and the final result of EI+WI (b). Note that even the EI results of $p=1$ are very different from that of $p=2$, the final result of EI+WI in this case is very similar to the case of $p=2$.

CONCLUSION

Envelope fluctuation and decay of seismic records carries ULF (ultra-low frequency) signals which can be used to estimate the long-wavelength velocity structure. We proposed a nonlinear seismic signal model: the "*modulation model*" for retrieving the ULF information in seismic waveform data. Eenvelope inversion based on least-square minimization of envelope data can recover the low-wavenumber components of unknown velocity strucutes (smooth backgrounds) so that the initial model dependence of waveform inversion can be reduced. This is demonstrated by the Marmousi model tests, in which a 1-D linear grandient starting model is used and the combined EI+WI (envelope-inversion plus waveform inversion) can correctively recover both the low- and high-wavenumber structure of the model. The other advantages of the envelope inversion are its independence to the source wavelet and its low cost (very little extra cost beyond the regular FWI cost). Futher study is needed for the inversion dependence on reflector distribution, acquisition aperture, and other limintations of the envelope inversion. The other important research topic for better understanding the advantages and limitations of envelope inversion is the forward modeling of envelope formation, which will be investigated in the future study.

Acknowledgments: We thank Mimi Dai, Jian Mao, Yu Geng, Lingling Ye, Rui Yan, Xiao-Bi Xie for discussions and helps. The suggestions and comments of reviewers are appreciated. We thank also the WTOPI members who participated in the discussions during our last year's annual WTOPI meeting. This research is supported by the WTOPI Research Consortium at the University of California, Santa Cruz.

APPENDIX

In this appendix we show how to derive the gradient of the envelope misfit as shown in equation (7).

First, calculate the gradient of the misfit as in equation (6) with respect to velocity, we obtain

$$\begin{aligned}\frac{\partial\sigma}{\partial v} &= \sum_{sr}\int_0^T E\cdot\frac{\partial\sqrt{y^2(t)+y_H^2(t)}^{\,p}}{\partial v}dt \\ &= p\cdot\sum_{sr}\int_0^T E\cdot\sqrt{y^2(t)+y_H^2(t)}^{\,p-2}\left[y(t)\cdot\frac{\partial y(t)}{\partial v}+y_H(t)\cdot\frac{\partial y_H(t)}{\partial v}\right]dt \\ &= p\cdot\sum_{sr}\int_0^T E\cdot e_{syn}^{p-2}\left[y(t)\cdot\frac{\partial y(t)}{\partial v}+y_H(t)\cdot\frac{\partial y_H(t)}{\partial v}\right]dt\end{aligned} \tag{A1}$$

Let us define the Hilbert transform of signal $f(t)$ as

$$H\{f(t)\}=h(t)*f(t) \tag{A2}$$

where

$$h(t) = \frac{1}{\pi t} \tag{A3}$$

Note that $h(-t) = -h(t)$. We then have

$$\begin{aligned}
&\int s(t)\delta H\{f(t)\}dt \\
&= \int s(t)\int h(t-t')\delta f(t')dt'dt \\
&= \int\int h(t-t')s(t)dt\delta f(t')dt' \\
&= \int\int h(-(t'-t)s(t)dt\delta f(t')dt' \\
&= -\int\int h(t'-t)s(t)dt\delta f(t')dt' \\
&= -\int H\{s(t)\}\delta(f)dt
\end{aligned} \tag{A4}$$

where δ means differention with respect to some kind of parameter.

Using the equation in above, then equation (A1) becomes:

$$\begin{aligned}
\frac{\partial\sigma}{\partial v} &= p\cdot\sum_{sr}\int_0^T E\cdot e_{syn}^{p-2}\left[y(t)\cdot\frac{\partial y(t)}{\partial v} + y_H(t)\cdot\frac{\partial y_H(t)}{\partial v}\right]dt \\
&= p\cdot\sum_{sr}\int_0^T\left[Ey(t)e_{syn}^{p-2}\cdot\frac{\partial y(t)}{\partial v} + Ey_H(t)e_{syn}^{p-2}\cdot\frac{\partial y_H(t)}{\partial v}\right] \\
&= p\cdot\sum_{sr}\int_0^T\left[Ey(t)e_{syn}^{p-2}\cdot\frac{\partial y(t)}{\partial v} - H\left\{Ey_H(t)e_{syn}^{p-2}\right\}\cdot\frac{\partial y(t)}{\partial v}\right]dt \\
&= p\cdot\sum_{sr}\int_0^T\left[Ey(t)e_{syn}^{p-2} - H\left\{Ey_H(t)e_{syn}^{p-2}\right\}\right]\cdot\frac{\partial y(t)}{\partial v}dt
\end{aligned} \tag{A5}$$

References

Almomin, A., and B. Biondi, 2012, Tomographic full waveform inversion: Practical and computationally feasible approach: 82nd Annual International Meeting, SEG, Expanded Abstracts, **31**, 1–5.

Baeten, G., de Maag, J.W., Plessix, R.-E., Klaassen, M., Qureshi, T., Kleemeyer, M., ten Kroode, F. & Zhang, R., 2013. The use of the low frequencies in a full waveform inversion and impedance inversion land seismic case study, *Geophys. Prospect.,* **61,** 701–711.

Bedrosian, E., 1962, A Product Theorem for Hilbert Transforms: Rand Corporation morandum, RM-3439-PR.

Biondi, B., and A. Almomin, 2012, Tomographic full waveform inversion (TFWI) by combining

full waveform inversion with wave equation migration velocity analysis: SEG Expanded Abstract.
Doi: 10.1190/segam2012-0275.1

Biondi, B and A. Almomin, 2013, Tomographic full waveform inversion (TFWI) by extending the velocity model along the time-lag axis, SEG Expanded Abstract, 1031-1034.

Bozdag, E, J., Trampert, and J., Tromp, 2011, Misfit functions for full waveform inversion based on instantaneous phase and envelope measurements: Geophys. J. Int., **185**, 845-870.

Brittan, J., J. Bai, H. Delome, C. Wang and D. Yingst, 2013, Full waveform inversion – the state of the art, *First break*, 31, 75-81.

Brown, J.L. Jr., 1986, A Hilbert transform product theorem: Proceedings of the IEEE, **74,** 520-521.

Chauris, H., D. Donno, H. Calandra, 2012, Velocity estimation with the normalized integration method, : 74th EAGE Conference & Exhibition, Expanded Abstracts, W020.

Claerbout, J. F., 1985, Imaging the Earth's interior: Blackwell Sci. Pub..

Clément, F., G. Chavent, and S. Gómez, 2001, Migration-based traveltime waveform inversion of 2-D simple structures: A synthetic example: Geophysics, 66, 845-860.

De Wolf, D. A., 1971, Electromagnetic reflection from an extended turbulent medium: Cumulative forward-scatter single-backscatter approximation: IEEE Trans. Antennas and Propagations AP-19, 254–262.

De Wolf, D. A., 1985. Renormalization of EM fields in application to large-angle scattering from randomly continuous media and sparse particle distributions: IEEE Trans. Antennas and Propagations AP-33, 608–615.

Donno, D., H. Chauris and H. Calandra, 2013, Estimating the background velocity model with the normalized integration method, 75th EAGE Conference & Exhibition, Expanded Abstracts.

Fichtner, A., Trampert, J., 2011. Resolution analysis in full waveform inversion. Geophys. J. Int. 187, 1604–1624.

Jannane, M., W. Beydoun, E. Crase, D. Cao, Z. Koren, E. Landa, M. Mendes, A. Pica, M. Noble, G. Roeth, S. Singh, R. Snieder, A. Tarantola, D. Trezeguet, and M. Xie, 1989, Wavelength of earth structures that can be resolved from seismic reflection data: Geophysics, **54**, 906-910.

Lailly, P., 1983, The seismic inverse problem as a sequence of before stack migrations, in Bednar, J. B., Redner, R., Robinson, E., and Weglein, A., Eds., Conference on Inverse Scattering:

Theory and Application, Soc. Industr. Appl. Math..

Ma, Y. and D. Hale, 2013, Wave-equation reflection traveltime inversion with dynamic warping and full-waveform inversion: Geophysics, **78**, R223-R233.

Mora, P. , 1989, Inversion=migration+tomography. *Geophysics*, **54**, 1575-1586.

Plessix, R., G. Baeten, J. W. de Maag, M. Klaassen, R. Zhang and Z. Tao, 2010, Application of acoustic full waveform inversion to a low-frequency large-offset land data set, SEG Expanded Abstract, 930-934.

Pratt, R. G., 1999, Seismic waveform inversion in the frequency domain, Part I: Theory and verification in a physical scale model: Geophysics, **64**, 888–901.

Pratt R.G., Song Z.M., Williamson P.R. and Warner M. 1996. Twodimensional velocity model from wide-angle seismic data by wavefield inversion. *Geophysical Journal International* **124**, 323–340.

Pratt, R. G., C. Shin, and G. J. Hicks, 1998, Gauss-Newton and full Newton methods in frequency-space seismic waveform inversion: *Geophysical Journal International*, **133**, 341–362.

Ravaut, C., S. Operto, L. Improta, J. Virieux, A. Herrero and P. Dell'Aversana, 2004, Multiscale imaging of complex structures from multifold wide-aperture seismic data by frequency-domain full-waveform tomography: application to a thrust belt, *Geophys. J. Int.,* **159,** 1032–1056.

Robinson, E. A., 1957, Predictive decomposition of seismic traces: Geophysics, **22**, 767-78.

Robinson, E. A., T. S., Durrani, and L. G., Peardon, 1986, Geophysical signal processing: Prentice-Hall International.

Shin, C. and Y.H. Ha, 2008, waveform inversion in the Laplace domain, *Geophysical J. International*, **173**(3), 922-931.

Sirgue, L. and Pratt, R.G. 2004, Efficient waveform inversion and imaging: A strategy for selecting temporal frequencies. *Geophysics*, **69**, 231–248.

Sirgue, L., Barkved, O.I., Dellinger, J., Etgen, J., Albertin, U. and Kommedal, J.H. 2010, Full-waveform inversion: the next leap forward in imaging at Valhall. *First Break*, **28** (4), 65–70. Shin, C., and Y. H. Cha, 2009, Waveform inversion in the Laplace-Fourier domain: *Geophys. J. Int*., **177**, 1067-1079.

Tarantola, A., 1984, Inversion of seismic reflection data in the acoustic approximation: Geophysics, 49, 1259-1266.

Tarantola, A., 1987, Inverse problem theory, Elsevier.

Tang, Y., S. S, Lee, A. Baumstein and D. Hinkely, 2013, Tomographically enhanced full wavefield inversion, 83rd Annual International Meeting, SEG, Expanded Abstracts

Virieux J. and Operto S. 2009. An overview of full waveform inversion in exploration geophysics. *Geophysics* **64**, WCC1–WCC26.

Vigh, D., J. Kapoor, N. Moldoveanu, and H. Li, 2011, Breakthrough acquisition and technologies for subsalt imaging: Geophysics, **76**, WB41-WB51.

Wang, F., H. Chauris, D. Donno & H. Calandra, 2013, Taking Advantage of Wave Field Decomposition in Full Waveform Inversion: 75th EAGE Conference & Exhibition, Expanded Abstracts.

Wu, R. S., 1994, Wide-angle elastic wave one-way propagation in heterogeneous media and an elastic wave complex-screen method: J. Geophys. Res., **99**, 751-766.

Wu, R. S., 2003, Wave propagation, scattering and imaging using dual-domain one-way and one-return propagators: Pure and Applied Geophysics, **160(3/4)**, 509-539.

Wu, R.S., B. Wu and M. Dai, 2012, Ultra-low-frequency information in seismic data : Its representation and extraction: MIP-report, MIP-23, 69-95, University of California, Santa Cruz.

Wu, R.S., J. Luo and B. Wu, 2013, Ultra-low-frequency information in seismic data and envelope inversion: SEG Extended abstract.

Xu, S., D. Wang, F. Chen, Y. Zhang, and G. Lambare, 2012, Full waveform inversion for reflected seismic data: 74th EAGE Conference & Exhibition, Expanded Abstracts, W024.